Catalysis Science & Technology

Accepted Manuscript

ROYAL SOCIETY OF CHEMISTRY

www.rsc.org/catalysis

Catalysis Science & Technology

PAPER

Tuning the CuxO Nanorod Composition for Efficient Visible Light Induced Photocatalysis†

Received 00th January 20xx,
Accepted 00th January 20xx

DOI: 10.1039/x0xx00000x

www.rsc.org/

Pradip Basnet,*[a] and Yiping Zhao[a]

A facile, low cost, and convenient method to fabricate Cu_xO (x = 1, 2) nanorod (NR) arrays is demonstrated by thermally oxidizing Cu NRs fabricated by oblique angle deposition. The single phase Cu_2O and CuO, and mixed phase Cu_2O/CuO polycrystalline NRs can be tuned simply by varying the thermal oxidation temperature. These Cu_xO NRs exhibit excellent visible light photocatalytic activity for both cationic (methylene blue) and anionic (methyl orange) dye degradation. When used as a photocathode, they also show good photoelectrochemical performance, especially the mixed phase Cu_2O/CuO NRs. The maximum stable photocurrent density is observed to be 0.24 mA/cm^2 under a simulated solar light. Incident photon-to-current efficiencies are found to be 20% and 44% at incident light wavelengths λ = 500 nm and 400 nm, respectively. These results show that the Cu_xO NRs fabricated through the oxidation method can be a suitable candidate for efficient visible light active photocatalysts for energy applications as well as for wastewater treatment.

Introduction

Visible light active photocatalysts (VLAPCs) have recently attracted tremendous attention for their renewable energy and environmental applications, such as wastewater treatment and bacterial inhibition.[1-4] Unlike traditional large bandgap photocatalysts, such as Titania (TiO_2), zinc oxide (ZnO), and tungsten oxide (WO_3) nanostructures, VLAPCs better utilize available solar irradiation ($\lambda \geq 400$ nm) for more efficient catalytic activity.[2, 3, 5] There are two general ways to generate efficient VLAPCs: either by modifying well known photocatalysts such that they absorb visible light by doping or constructing heterostructures,[6, 7] or by exploring the photocatalytic properties of new materials with small energy band gaps, such as CuO, Cu_2O, α-Fe_2O_3, CoO, Bi_2O_3, $BiVO_4$, *etc*.[8-12] Among these small bandgap materials, copper oxides (Cu_xO; x = 1, 2) hold great potential due to their unique optical and charge transport properties.[11, 13-15] Cu_2O and CuO, both p-type semiconductors, are suitable for visible light absorption because of their favorable bandgap values that range from 1.7 to 2.6 eV.[13, 16] Cu_2O is considered more attractive for photocatalysis since its conduction band lies just above the water reduction potential (0 V *vs* NHE), and its bandgap is about 2.0 – 2.2 eV, which is larger than the water oxidation potential, 1.23 eV, but remains in the visible region.[8] In addition to photocatalysis, Cu_2O and CuO nanostructures have been studied for solar energy conversion,[9] antimicrobial applications,[10] gas-sensing,[17] and lithium-ion batteries.[14, 18] The use of Cu_2O nanostructure as photocathode is also promising due to its favorable energy band positions, with the conduction band (CB) lying more negative than the H_2 evolution potential and the valance band (VB) lying just positive of the O_2 evolution potential.[1, 19] However, there are a limited number of reports describing the photoelectrochemical (PEC) properties of Cu_xO nanostructures, and those that do exist indicate that the stability of Cu_xO nanostructures could be a potential problem for light related applications. This is because the redox potential for Cu_2O reduction exists within its bandgap, and theoretically Cu_2O can be reduced to Cu by photoexcited electrons, which causes photo-reduction/corrosion.[1, 28-30] Thus, there are several conflicting reports appearing in literature. For example, Yu *et al*. studied CuO/Cu_2O microspheres for methyl orange (MO) degradation under visible light irradiation and reported no significant photocatalytic degradation was achieved unless aided with H_2O_2 as a hole scavenger.[16] On the other hand, Zhou *et al*. [20] and Chen *et al*.[18] separately reported excellent photocatalytic activity of Cu_2O/Cu nanocomposites and Cu/Cu_2O core-shell nanowires for dye degradations of MO and methylene blue (MB). Hara *et al.* has reported on a lengthy water splitting test on Cu_2O powders under solar irradiation and observed no noticeable activity loss for 1900 hours.[9] Later Jongh *et al*. published a paper questioning the stability of Cu_2O nanostructure for PEC water splitting *via* normal photocatalytic reaction.[21] Since then, several other papers have been published showing differing results on the photocatalytic stability of Cu_2O.[19, 22-24] In addition, Paracchino *et al.*, and Zhang *et al.*, have independently studied the stability of Cu_2O with and without the protecting layers of Al/ZnO/TiO_2 and CuO.[1] Their results have shown that photocatalytic stability of Cu_2O nanostructures with the coatings has been enhanced. Interestingly, Zhang *et al.* has interpreted the enhanced stability due to the crystallographic orientation of Cu_2O along [111] plane.[29] The exact reason for these conflicting observations is not clear yet. Recently, Bendavid and Carter suggest that the stability of Cu_2O nanostructures are closely related to their crystallographic orientations,[25] which implies that the Cu_xO fabrication technique may play a dominant role.

[a] *Department of Physics and Astronomy, and Nanoscale Science and Engineering Center, University of Georgia, Athens, Georgia 30602, USA.*
*E-mail: pbasnet@physast.uga.edu; Phone: (706) 542-6230; Fax: (706) 542-2492.
†Electronic Supplementary Information (ESI) available: (1) Transmittance (%*T*) and Reflectance (%*R*) spectra of Cu_xO NRs, (2) Tauc's plot for direct and indirect bandgap calculations, (3) self-degradation of MB and MO dyes under visible light illumination, (4) estimation of pseudo-first order dye degradation rates, (5) H_2O_2 assisted photocatalytic activity, (6) decolorization/mineralization tests towards oxidation, (7) stability tests for Cu_xO NR samples. See DOI: 10.1039/x0xx00000x

Both wet chemical methods, such as electrodeposition,[22, 23] hydrothermal synthesis,[26] sol-gel,[27] and vapor-phase based methods such as thermal oxidation,[28, 29] sputtering,[30] microwave irradiation,[31] direct oxidation in air,[32] and physical vapor deposition (PVD),[28] have been reported to prepare the Cu_xO nanostructures. Among these techniques, PVD is a versatile, reliable, low cost, and fast deposition technique for the fabrication of thin films and nanostructures. In particular, PVD is advantageous based on the fact that one can control the porosity of nanostructured thin films when the system is arranged into an oblique angle deposition (OAD) configuration.[4, 28, 33] OAD is a simple and well-known technique in which the incident material vapor is directed toward a substrate at large incident angles (> 70°) with respect to substrate surface normal, resulting in self-organized, aligned, and tilted nanorod (NR) arrays.[4, 34] The growth of NRs is controlled by the geometric shadowing effect and surface diffusion of vapor adatoms. Detailed descriptions of the growth process can be found in some recent review articles.[35] Our previous works have proven that the OAD deposition is a versatile method in fabricating efficient polycrystalline photocatalyst NRs.[4, 7, 34, 36, 37] It is expected that aligned and polycrystalline Cu_xO NR arrays would have different photocatalytic activities if their crystalline phase and compositional properties could be changed and tuned, and the relative stability problem could also evolve with the crystal phases.

In this report, a facile fabrication method of Cu_xO NRs based on OAD is demonstrated. The sample preparation strategy is to first deposit the Cu NRs using the OAD technique, then to oxidize the as-prepared Cu NRs in the ambient condition for a predetermined time at a given temperature. Depending on the oxidation temperature, one can obtain the single phase Cu_2O, and CuO, or the mixed phase Cu_2O/CuO NRs. The visible light induced photocatalytic activities of these Cu_xO NRs are investigated for degradations of both the cationic (MB) and anionic (MO) dyes. In addition, with the help of small amount of H_2O_2, a significant increases in the degradation rates are observed for both the MB and MO dyes. The PEC properties and stability of the Cu_xO NR samples are strongly dependent on applied bias potentials. All the nanostructures are stable for photodecay test, but in PEC measurements under the visible light illumination and at a negative bias potential, the photocurrents from all the samples degrade with illumination time. The CuO NR sample is relatively more stable than the other two samples, while the Cu_2O NR sample is the least stable.

Results and Discussion

Morphology and structural properties

Fig. 1(a) shows the representative top and cross-sectional view SEM images of as-deposited Cu NR samples. Morphology related parameters such as the direction of vapor incident angle θ, NR tilting angle β, NR vertical thickness h, and NR diameter D are also defined in Fig.1(a). Fig. 1(a) reveals that the as-prepared Cu nanostructure consist of well-aligned and tilted NRs. From the top-view SEM image, the NR density η is estimated to be η = 50 ± 10 rods/ μm^2. These NRs are straight and exhibit relative smooth side surface, which is consistent with the result reported by Li. *et. al*.[28] The cross-sectional image in Fig. 1(a) shows that the Cu NRs are of nearly cylindrical shape with increasing diameter towards the top. The average width (or diameter) of the NRs near the top is D = 40 ± 10 nm. To make a fair comparison, we measured the diameters of both the Cu and Cu_xO NRs at about 100 nm below the top surface. Those Cu NRs are tilting away from the substrate normal at β = 70 ± 5° and h = 350 ± 20 nm. The measured value of β does not match with the angle predicted by both the tangent rule,[38] β = arctan(1/2 tan θ) = 82°; and cosine rule,[39] $\beta = \theta$ – arcsin((1-cos θ) /2) = 58°, for OAD. However, the material dependent models described in the literature can be used to explain the resulting β angle.[40] Fig. 1(b) to (d) show the representative SEM images for Cu_xO NR samples obtained at oxidation temperature T = 150, 240, and 380°C, respectively. Compared to Fig. 1(a), the changes in morphology of Cu_xO NR samples are obvious; visually one can see that the NR diameter becomes larger after oxidation, which is expected. Other morphological parameters, such as h, β, and η are also changed, and the results are summarized in Table 1. The increase in diameter could be interpreted as oxidation and coarsening of NRs with increasing oxidation temperature. As a result, the NR density is found to be decreased with T. Regardless of the oxidation temperatures, the β values are observed to be almost unchanged.

The crystal structures of Cu_xO NRs are characterized by XRD. Fig. 2(a) shows the XRD patterns of Cu_xO NR samples oxidized at different temperatures. XRD pattern of the as-deposited Cu NRs (Fig. 2(a)) is also included as a reference, and the result shows that those samples are polycrystalline Cu with no detectable impurities (as compared with JCPDS Ref. No. 085-1326). All the diffraction peaks of the sample oxidized at T = 150 °C, namely at 2θ = 29.58°, 36.44°, 42.33°, 61.41°, and 73.56°, are consistent with the diffraction patterns of Cu_2O (JCPDS Ref. No. 078-2076), representing the Cu_2O crystal planes of (110), (111), (200), (220), and (311), respectively. While the sample oxidized at T = 380 °C is composed of pure single phase CuO (JCPDS No. 048-1548) as confirmed by the peaks at 2θ = 32.51°, 35.42°, 35.54°, 38.71°, 38.90°, 48.72°, 53.49°, 58.26°, 61.53°, 65.81°, 66.22°, 67.90°, 68.12°, 72.37°, 74.98°, and 75.24°, which represent the (110), (002), (11$\bar{1}$), (111), (200), (20$\bar{2}$), (020), (202), (11$\bar{3}$), (022), (31$\bar{1}$), (113), (220), (311), (004) and (22$\bar{2}$) crystal planes of CuO. Nevertheless, all the samples oxidized in the temperature range, 150 °C < T < 380 °C, indicate the presence of a mixture of Cu_2O and CuO phases, which is consistent with the thin film results reported in literature.[15, 16]

The phase evolution and nanocrystal growth of Cu_2O and CuO NRs can be further understood through detailed XRD analysis. First, the average crystalline sizes can be estimated using the most prominent peaks of Cu_2O (111), CuO (111), and CuO (11$\bar{1}$) planes by the Scherrer's equations, $d = K\lambda / \beta' \cos\theta$, where d is the diameter of the crystalline grain, K = 0.9, λ (Cu-Kα1) = 1.5405980 Å, and β' is the full width at half maximum (FWHM) of the selected diffraction peak. Note that the accurate estimation of the real crystalline size of each samples need to know the line broadening due to XRD instrument and the lattice strain/ disorder using standard reference material. According to Suryanarayana, one can use the raw XRD data to compare the trend of change of crystallite size as we are interested in the relative structural changes for different oxidation temperature.[41] Results of the estimated crystallite sizes are summarized in Table 2. Overall, the estimated crystalline sizes of Cu_2O and CuO increase with T (with the exception for the sample annealed at T = 290 °C and 340 °C). This deviation could be attributed to the peak broadening due to

the phase change from Cu_2O to CuO, i.e., changing the XRD peak position from 2θ = 36.44° of Cu2O to 35.42° and 35.54° of CuO (see Fig. 2(a)). Besides, a general trend of increasing the estimated crystallite size of CuO at higher T is in good agreement with the observed NR coarsening.[18] In addition, the XRD data can also be used to roughly estimate the Cu_2O/CuO composition ratio through a semi-quantitative analysis utilizing the Rietveld program using the FullProf software as described in the literature.[42, 43] The use of Rietveld procedure (whole profile) can be considered as a reliable method to estimate the weight percentage (wt %) of each component in the mixture. Fig. 2(b) shows the relative wt % of Cu_2O and CuO for different oxidation temperatures. The Cu_2O wt % in the Cu_xO NR samples oxidized at T = 150, 190, 210, 240, 290, 340, and 380°C is estimated to be 100%, 96%, 92.5%, 53%, 21.6%, 9.2%, and 0%, respectively. This results can also be confirmed by using ratios of the most prominent peaks of Cu2O (111) and CuO (111), as described in the literature.[16] The estimated results are shown by a blue line in Fig. 2(b). The increased amount of CuO with oxidation temperature is reasonable since more and more Cu_2O are oxidized into the more stable CuO phase at higher T. It is also expected that such an oxidation process starts from the outer surface of the Cu_2O NRs and progresses inwards.

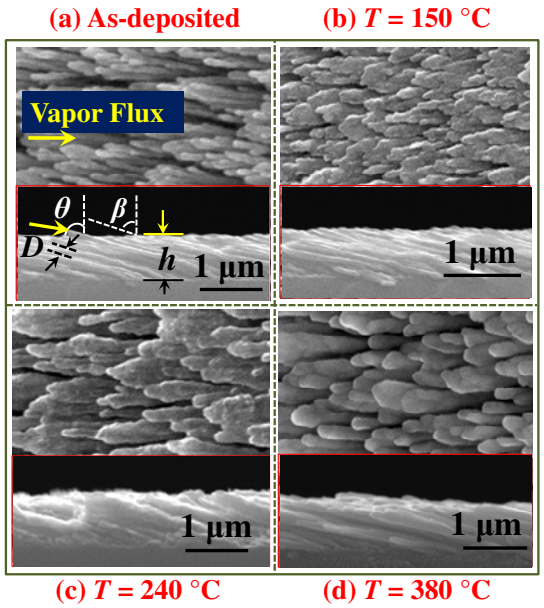

Figure 1. Top-view SEM images of (a) as-deposited Cu NRs, (b) Cu_2O NRs, oxidized at T = 150°C, (c) Cu_2O/CuO NRs, oxidized at T = 240°C, and (d) CuO NRs, oxidized at T = 380°C. Figure insets represent their respective cross-sectional views.

Table 1. Summary of SEM images analysis for morphology of Cu and Cu_xO NRs.

	As-deposited Cu	T = 150 °C Cu_2O	T = 240 °C Cu_xO (mixed)	T = 380 °C CuO
NR Tilting angle, β (°)	70 ± 5	70 ± 5	70 ± 5	74 ± 5
NR Thickness, h (nm)	350 ± 20	340 ± 20	340 ± 20	320 ± 20
Density, η (#/μm^2)	50 ± 10	45 ± 10	45 ± 10	40 ± 10
NR diameter, D (nm)	40 ± 10	50 ±10	60 ± 10	70 ± 10

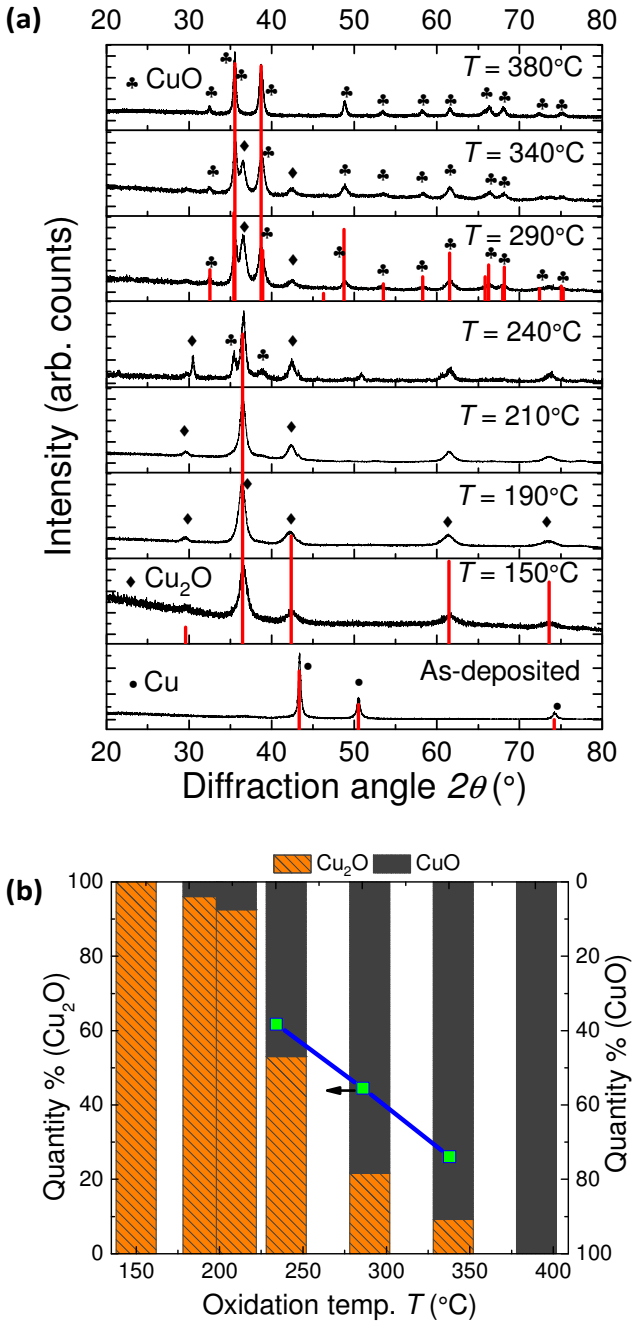

Figure 2. (a) Comparison of XRD patterns of as-deposited Cu and oxidized Cu_xO NR samples, and (b) the change of the Cu_2O and CuO composition ratio in the Cu_xO NR samples, estimated through XRD patterns, as a function of oxidation temperature T.

Optical properties

The appearance of an as-deposited Cu NR sample and some representative oxidized Cu_xO NR samples are shown in inserts of Fig. 3(a). The Cu NR sample is optically opaque and highly reflective by visual inspection. After oxidation, the Cu_xO NR samples appear to be pale yellowish in color at lower T (≤ 240 °C) and then change slowly into darker reddish black with

increasing *T* (240 °C ≥ *T* ≤ 380 °C). This shows that the visible light absorption of the sample is increased at higher *T* values. The optical absorbance spectra (*A*) of the Cu_xO NR samples are obtained by measuring both the transmittance (%*T*') and reflectance (%*R*) spectra,

$$A = \alpha \cdot h = \ln\left(\frac{1-R}{T}\right), \quad (1)$$

where *α* and *h* are the absorption coefficient and thickness of the film, respectively. Representative transmittance and reflectance spectra of the Cu_xO NR samples are shown in Fig. S1 in supporting information (SI), and the estimated UV-Vis absorbance spectra of these samples are shown in Fig. 3(a). The absorption edges of the oxidized samples are red-shifted with increasing *T* (with an exception for the sample oxidized at *T* = 190 °C). This general trend can be attributed to the crystal phase change, as confirmed by the XRD results. The optical bandgaps of those Cu_xO NR samples are estimated using the Tauc plots with the following relationship,

$$A\varepsilon = A_0\left(\varepsilon - E_g\right)^m, \quad (2)$$

where *ε* is the photon energy, A_0 is a constant relative to the material, and *m* is an exponent indicating a direct bandgap material (*m* = 1/2) and an indirect bandgap material (*m* = 2).[4,14] As reported by the literature, Cu_xO could exhibit both direct and indirect band gaps behaviors.[14, 15] Therefore, Tauc's plots are obtained for both the direct and indirect allowed transitions. Fig. 3(b) shows an example of the Tauc's plots for Cu_2O NR sample at *T* = 150 °C. The direct and indirect bandgaps of Cu_2O NRs are determined to be E_g^D = 2.54 and E_g^I = 2.02 eV, respectively. The Tauc's plots for all other Cu_xO NR samples are shown in Fig. S2(a) - (b) in SI; and the resulting bandgap values are summarized in Table 2. Results show that the single phase Cu_2O and the mixed phase Cu_2O/CuO samples exhibit both the direct and indirect bandgaps while the single phase CuO NR samples only exhibit a direct transition (see Fig. S2(b) in SI). The direct bandgap of the single phase CuO NRs is 2.13 eV. Similar phenomenon for the Cu_2O and CuO films have been reported by Heinemann *et. al*., and Zoolfakar *et. al.*[14, 15] The estimated direct bandgap values of Cu_2O NRs (E_g^D = 2.54 eV) are in good agreement with the results reported for Cu_2O thin films which are in the range of E_g = 2.1-2.6 eV.[12, 15, 29] However, the estimated values for indirect bandgaps of our Cu_2O NR samples are slightly lower than those reported in the literature (2.1 -2.21 eV).[14, 15] These observed lower values could be due to various reasons, such as heat treatment (during oxidation), change or restriction in grain sizes during crystal phase change occurred, composition of mixed phases, *etc*., as reported by Zoolfakar *et al*.[14]

Photocatalytic activity

The photocatalytic dye degradation (PDD) of both the MB and MO aqueous solutions are tested to characterize the catalytic activity of Cu_xO NR samples under visible light irradiation. The reason for choosing MB and MO dyes is that they are the two most popular dyes for photocatalytic activity test, and one (MB) is cationic and one (MO) is anionic.[44, 45] Different Cu_xO NR samples could exhibit different intake capacity *via* dark adsorption. Two control experiments are performed. First experiment is to monitor the dark adsorption of dyes onto the Cu_xO NRs by keeping the dyes in dark with Cu_xO samples for 30 to 60 mins. No significant dark adsorption of both the dyes are observed with all the Cu_xO NR samples. Second is to investigate the direct photodecay of the dyes by irradiating the light to the dye solutions without the Cu_xO samples. We observed a slow decrease in absorption spectra of MB solution but no obvious change for MO solution (see Fig. S3(a)-(b) in SI). The decay rate constant for MB is estimated to be k_{light}^{MB} = 0.003 ± 0.001 hr^{-1}. This result suggests that there is a self-degradation of MB under visible light irradiation. The plots of MB and MO absorption peak versus illumination time are shown in Fig. S4(a)-(b) in SI, and the decay constant κ_c value extracted from these plots as a function of Cu_2O weight percentage γ is plotted in Fig. 4. Note that γ decreases monotonically with *T*. We observe two trends: first, the photodecay rates κ_c for both MB and MO follow the same trend with respect to γ (or *T*); second, the MB degradation rates are relatively higher than those of the MO degradation rates. It is clear that under the same testing conditions, the single phase CuO NR samples give the lowest photocatalytic performance for both the cationic and anionic dyes while the single phase Cu_2O NR samples show relatively high κ_c. Such a difference can be explained by the amount of reactive oxygen species (ROS) produced on the surface of photocatalyst.[46] The generation of ROS is strongly dependent on the amount of photogenerated CB electrons and VB holes, and more importantly on the redox potentials of a photocatalyt (see Figs. 5(a) and (b)). The higher ROS generation rate can be expected if the CB edge is more negative and the VB edge more positive (see Fig. 5(b)). Thus, the low degradation rate with the single phase CuO NR sample compared to that of single phase Cu_2O NR sample could be due to its CB edge lying in a position unfavorable for multiple electron transfer (see Fig. 5(b)).[22] For CuO sample, its CB edge is approximately located at +0.0 to 0.03 V (V *vs* NHE) while the required O_2 reduction potential is -0.28 V as shown in Fig. 5(b).[47] Therefore, the CB location could not provide a sufficient potential to reduce the molecular O_2 through electron transfer, $O_{2(ads)} + e^- \rightarrow O_2^{\bullet-}$.[48, 49] But its VB edge is located more positively than the H_2O oxidation potential (+1.23 eV), which can generate hydroxyl radical, $OH^-_{(ads)} + h^+ \rightarrow OH^{\bullet}_{(ads)}$, leading to the generation of hydrogen peroxide, $2OH^{\bullet} \rightarrow H_2O_2$. Overall, this results a low efficiency in generating ROS. In contrast, the single phase Cu_2O samples have a more negative CB edge, reported to be located at -1.2 to -1.4 V (V *vs* NHE), and its VB edge located around +1.1 to +1.3 V (V *vs* NHE) (deduced from the bandgap), which is potentially for higher ROS generation rate.[47, 49]

When *T* increases from 150°C to 210°C, the γ changes slightly, from 100% to 92.5%, and the photodecay rate also decreases slightly by considering the error bar in the measurements. This is due to the phase transition of Cu_2O to CuO. When *T* reaches to 240°C, γ becomes 53% and k_c increases from ~ 0.06-0.07 hr^{-1} to ~ 0.084 hr^{-1}. Such an increase in k_c could be due to the competition of the reduced amount of Cu_2O and the increased Cu_2O/CuO interface. By changing Cu_2O to CuO, the photodecay rate k_c is expected to decrease as discussed above. However, since part of Cu_2O is converted into CuO, there will be an increased amount of Cu_2O/CuO interfaces formed. Due to the different bandgap and CB/VB locations of Cu_2O and CuO, a heterostructure is formed at these interfaces, which could take the advantages of the

energy band miss-alignment of both the Cu_2O and CuO. As shown in Fig. 5(a), at the Cu_2O/CuO interface, a charge separation process could occur: the CB electrons of higher energy from Cu_2O can move to the CB of CuO (lower energy) while the VB holes from CuO could transfer to the VB of Cu_2O (energetically favorable). In these processes, the Cu_2O sample acts as an electron donor and hole acceptor while the opposite applies for CuO sample. Charge separation at the interface of the mixed phase Cu_2O/CuO samples is very advantageous in extending the life-time of photogenerated electron-hole pairs, to avoid their recombination, which may result in an enhanced PDD activity.[5, 50] Similar mechanisms have described in the literature for heterojunction of metal oxides semiconductors.[16, 18, 37] Our experimental observation infers that when T increased from 150°C to 240°C, the effect of hetero-interface or charge separation will surpass the effect caused by the phase transition from Cu_2O to CuO, and give a net increase in k_c when T increased to 240°C. However, when T increases further (> 240°C), more Cu_2O changes to CuO, and the amount of Cu_2O/CuO interfaces should decrease eventually, less charge separation is expected, which results in a lower k_c. In the meantime, more Cu_2O is changed into CuO, which also induced a further reduction in k_c. Both effects result in a faster loss in k_c values after T > 240°C and bring about the almost linear decrease of k_c with respect to γ as shown in Fig. 4.

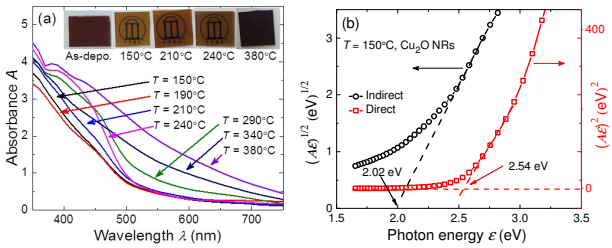

Figure 3. (a) Absorption spectra of CuxO NR samples, and (b) the representative Tauc's plot showing a direct and an indirect bandgap for the Cu2O NR sample. Insets in (a) show the digital photographs of CuxO samples oxidized at different T, placed over the University of Georgia logo.

Table 2. Structural and optical parameters of Cu_xO NR samples.

	Structural parameters		Optical parameters	
Sample	Estimated grain size (nm) at (111), Cu_2O phase	Estimated grain size (nm) at (111) /(11 $\bar{1}$), CuO phase	Direct bandgap	Indirect bandgap
T = 150 °C	6.4	--	2.54	2.02
T = 190 °C	7.7	--	2.51	2.04
T = 210 °C	8.5	--	2.50	2.06
T = 240 °C	9.2	--	2.50	1.94
T = 290 °C	--	12.8 / 7.6	2.45	2.16
T = 340 °C	--	17.0/ 10.4	2.24	--
T = 380 °C	--	19.9/ 14.3	2.13	--

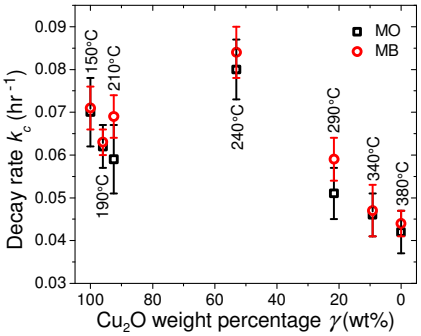

Figure 4. Photocatalytic decay rates k_c as a function of Cu_2O weight percentage γ, obtained at different T, for MO and MB degradation under visible light illumination.

In order to explain the difference in decay rates of MB and MO, we need to consider the role of dyes played in the photodecay characterization. According to the literature, the overall photocatalytic activity observed are governed by two pathways, the direct semiconductor photoexcitation and indirect dye photosensitization.[51] The latter process of photosensitization (also called photo-assisted degradation) involves a two-step process: excitation of dye *via* visible light absorption and transfer/injection of excited electron(s) onto the CB of a photocatalyst as shown in Fig. 5(a).[52] For this process, the amount of light absorbed by individual dye determines the indirect photosensitization process and hence contribute for the total decay rate. It is expected that under the same experimental conditions, the more light absorbed by a dye, the higher the photodecay rate. Therefore, we compare the absorbance spectra of the dye solutions, the Cu_xO NR samples, and the emission spectrum of the light source used for the photocatalytic experiments. As seen from the Fig. 6, the MB absorbs the light in the wavelength range of 550 to 700 nm (λ_{max} at 664 nm) while MO absorbs light from 380 to 530 nm (λ_{max} at 465 nm). MB has a larger absorption band and the source light covers entire MB absorption spectra. As a consequence, more photoexcited electrons are expected to be injected into the CB of photocatalyst resulting in a higher MB degradation rate. As described above, the self-degradation of MB solution may also contribute to the higher decay rates.

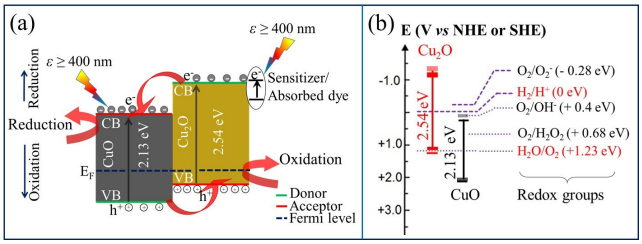

Figure 5. The proposed mechanism for the enhancement of the photocatalytic activity for MB and MO with the mixed phase Cu_2O/CuO NR samples. (a) Generation and transfer of charge carriers. Note that the electrons and holes transfer direction for Cu_2O/CuO composites are shown by red arrows, and (b) energy band edges of single phase Cu_2O and CuO NRs with redox couples in water.

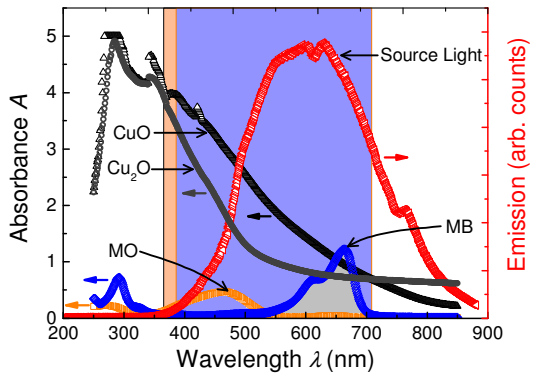

Figure 6. The comparison of the absorbance spectra of Cu_xO NR samples, and dye absorbance spectra (MO & MB) as well as the emission spectrum of illuminating light.

To confirm the stability of the Cu_xO NR samples in PDD reactions, MB and MO degradation experiments are repeated for three successive cycles for each of the CuxO sample. Then the XRD patterns, UV-Vis transmittance, and the decay rates after each test and with reference to the fresh sample, are used to compare their stability. Fig. S8 in SI shows the representative results of MB degradation with Cu_2O NR sample, used for total 21 hrs of experiments. The photocatalytic activities are observed to remain about the same (less than 5% change in the total degradation), indicating that the prepared Cu_2O NR samples are stable in aqueous solution and under visible light irradiation. Similarly, other Cu_xO NR samples also retained their photocatalytic activity after multiple experiments. Figs. S9 and S10 in SI show a representative XRD patterns and the UV-Vis transmittance spectra of some selected Cu_xO NR samples respectively, *i.e.* before and after the dye degradation experiments. No changes in the crystal structures and optical absorbance are observed under the detection limit of instruments, indicating these Cu_xO NR samples are fairly stable during the photocatalytic reaction in aqueous solution. These results could be attributed to the dominated crystallographic orientation of Cu_2O, *i.e.* along the plane [111] as confirmed by the XRD (see Fig. 2(a)).[22, 25] While the stability for mixed phase Cu_2O/CuO and the single phase CuO samples are in good agreement with the literature: single phase CuO is reported to be the most stable and it also improves the stability of Cu_2O by acting as a protecting layer.[22, 24]

Furthermore, in order to make a fair comparison of the dye degradation efficiency of our best sample (Cu_2O/CuO NRs, T = 240°C) with the literature we used the optimized amount of H_2O_2, *i.e.*, 0.01:3 H_2O_2 to dye volume ratio (v/v) suggested in the literature,[53] and tested the photodecay performance for both MB and MO solutions. Significant enhancements have been observed in the degradation rates for both dyes, resulting 90% and more decolorization of both MO and MB in 7 hrs (see Figs. S5 (a)-(d) and S6 (a)-(d) in SI). These enhancements are about 5.4 and 3.7 times compare to the decay rates of MB and MO without the use of H_2O_2 (see Figs. S5 (d) and S6(d) in SI), and these values are much higher than the reported value for MO degradation (~ 14% removal of MO in 5 hrs) with mixed phase Cu_2O/CuO hollow microsphere.[16] It is important to note that in Ref. 16, the authors have used 0.2 g of Cu_2O/CuO powder in the 20 ml of MO aqueous solution with similar initial concentration (31 µM) we used, but the light intensity is relatively low (0.46 mW/cm^2).

We further tested the final dye solutions obtained from these experiments to indirectly confirm the permanent composition change (see Fig. S7 (a) - (d) in SI). Purging oxygen (~10 sccm) to the solutions for 30 mins did not reversibly change the dye color back at least for 2 hrs, so we believe that the photocatalytic reaction mechanisms are dominated by the complete mineralization, but not by forming the leuco MB and protonated MO *via* charge transfer.[54, 55] The observed results that are best fitted with the Langmuir-Hinshelwood kinetic model further validated the above conclusion regardless the use of H_2O_2.[50, 55]

Photoelectrochemical (PEC) properties

The cyclic voltammetry (CV), dynamic photoresponse, and incident photon-to-current efficiency (IPCE) measurements are performed to characterize the PEC properties of Cu_xO NR samples.[1] Three representative samples, namely, a single phase Cu_2O NR sample (T = 150°C), a mixed phase Cu_2O/CuO NR sample (T = 240°C), and a single phase CuO NR sample (T = 380°C), are characterized. Multi-cycle CV measurements are used to determine the redox potentials, and the stability of these samples in the electrolyte solution. Some of the selected cyclic voltammograms are shown in Fig. 7 (a) to (c). Three different scanning rates, 100 mV/s, 50 mV/s, and 10 mV/s, are chosen to confirm if any oxidative and reductive peaks are missing at the highest scan rate. Unless otherwise stated, here we show the cyclic voltammograms results from -0.6 to + 0.6 V obtained from a scan rate of 100 mV/s. As seen in Fig. 7(a) to (c), over the entire potential range, both the cathodic and anodic peaks are observed for all three samples. The single phase Cu_2O and the mixed phase Cu_2O/CuO NR samples are observed to be relatively unstable for the first few minutes (Figs. 7(a) & (b)), but stabilized in about 10 minutes while the CuO NR sample is observed to be the most stable one (see Fig. 7(c)). The cathodic and anodic peaks for Cu_2O NR sample are observed at the potentials V_c = -0.16 V, V_c = -0.42 V, and V_a = +0.52 V, which are consistent with the reported characteristic reduction and oxidation peaks of Cu_2O and CuO.[22] For the mixed phase Cu_2O/CuO NR sample, with the increased number of cycles, initially the observed V_a = +0.25 V moves towards more positive values as shown in Fig. 7(b) while the V_a = +0.01 V almost disappeared. The CV of CuO NR sample exhibits only one cathodic (V_c = -0.39 V) and one anodic (V_a = +0.25 V) peaks (Fig. 7(c)). The observed variations in the voltammograms, for different samples, demonstrate that the stability of Cu_xO NRs are strongly phase dependent where the CuO NR sample exhibit the most stable phase. These results are in good agreement with the report by Zhang *et. al.*, who have reported an enhanced stability of Cu_2O nanostructures by coating a protecting thin layer of CuO.[24] For Cu_2O NR sample, the maximum stable cathodic and anodic current density values are observed to be J_c = 0.38 mA/cm^2 and J_a = 0.85 mA/cm^2, respectively. Further, it is observed that the cathodic current density decreases beyond V_c = -0.16 V until it reach another

plateau at V_c = -0.42 V where the cathodic current becomes stabilized to J_c = 0.31 mA/cm². For the mixed phase Cu_2O/CuO sample, the maximum cathodic and anodic current densities are J_c = 0.82 mA/cm² and J_a = 1.2 mA/cm², respectively. Beyond the cathodic peak, V_c = -0.36 V, for $V \leq$ -0.5 V, J_c is observed to increase almost linearly with the applied potential. The maximum stable cathodic and anodic current densities for single phase CuO NR sample are J_c = 0.5 mA/cm² and J_a = 0.35 mA/cm². The J_c - V_c also shows a linear relationship for $V \leq$ -0.5 V. This linear behavior for the both single phase Cu_2O and mixed phase Cu_2O/CuO samples could be attributed to the increased reduction while the absence in Cu_2O NR sample could be due to the diffusion control current.[56]

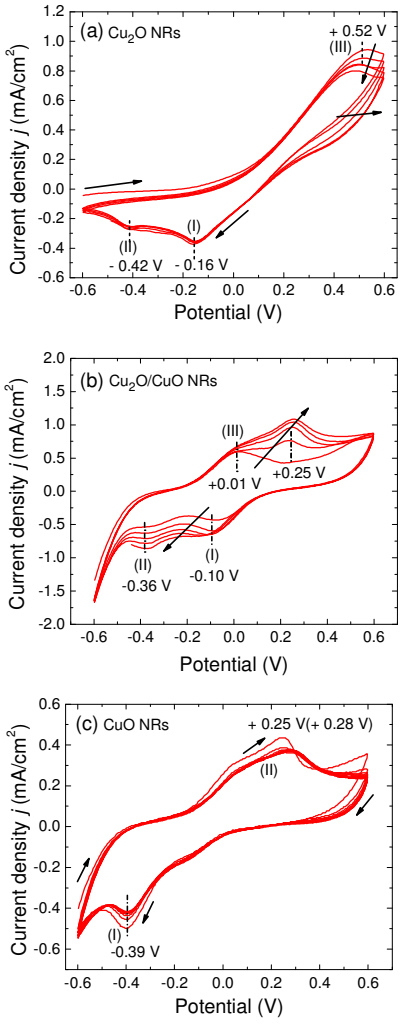

Figure 7. The CV curves of selected Cu_xO NR samples: (a) Cu_2O (T = 150°C), 5 cycles; (b) Cu_2O/CuO (T = 240°C), 5 cycles; and (c) CuO (T = 380°C), 10 cycles.

Fig.8 (a) shows the dynamic photocurrent generation curves, the photocurrent density J_{ph} versus time t, for three samples tested in 0.5 M Na_2SO_4 at a bias potential of V_c = -0.5 V and under the illumination of AM 1.5G. The chopping frequency is 0.033 Hz. The observed photo-induced cathodic currents demonstrate the p-type semiconductor nature of these samples.[23, 56] For all the three samples the J_{ph} - t curves show that the initial J_{phs} are large, and then decrease with chopping times, which is consistent with the results from most of the PEC measurements. Note that the J_{ph} decays for single phase Cu_2O sample and the mixed phase Cu_2O/CuO sample relatively quickly, while for the single phase CuO sample, J_{ph} decreases much slower (see Fig. S11 in SI). After 15 minutes, we observed about 15% loss in photocurrent for Cu_2O, about 33% for mixed phase Cu_2O/CuO, and only 2% for CuO NR sample. The single phase Cu_2O sample shows the lowest stable J_{ph} = 0.06 mA/cm² while the Cu_2O/CuO sample demonstrates the highest J_{ph} (= 0.24 mA/cm²). The CuO sample has moderate J_{ph} = 0.18 mA/cm². This result is consistent with the observed PDD results, discussed in previous section, except for the single phase CuO and Cu_2O samples. The main reason for mixed Cu_2O/CuO sample to have the maximum J_{ph} could be due to the charge separation effect at the Cu_2O/CuO interface, as explained above. The applied negative bias to the single phase CuO sample causes its CB to move towards more negative, resulting in an enhanced J_{ph} values. Similar argument can be applied to the single phase Cu_2O sample where a more negative CB location far beyond the O_2 reduction potential results in a low reaction efficiency, hence a lower photoresponse.[27, 57]

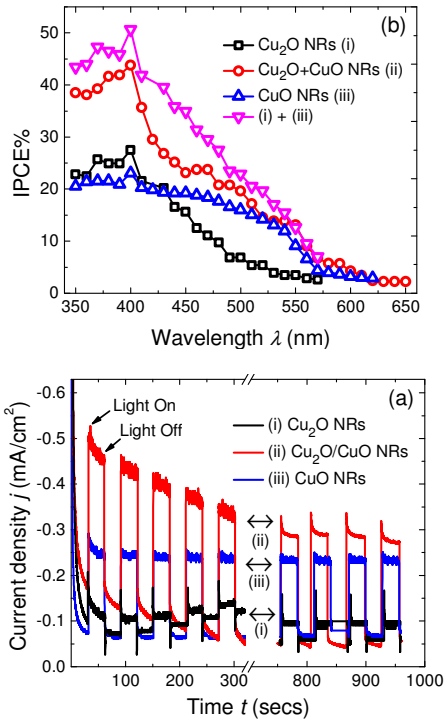

Figure 8. (a) Photocurrent response and (b) IPCE spectra of selected Cu_xO NR samples (cathode) in 0.5 M Na_2SO_4 solution under solar simulator (1 sun) at -0.5 V *vs.* Ag/AgCl.

The IPCE spectra for the three samples are shown in Fig. 8(b) for the bias V_c = -0.5 V. As expected, the overall higher IPCE% is observed for the mixed phase Cu_2O/CuO NR sample:

the highest IPCE% value is estimated to be 44% at λ = 400 nm and it decreases monotonically with increase of wavelength. At λ = 550 nm, the IPCE is still about 10% which indicates that the most of the visible photons have been successfully converted into photocurrents. The IPCE values for Cu_2O and CuO NR samples are observed almost the same and remain as a constant (20 - 27%) in a wavelength regime of $\lambda \leq 430$ nm. The Cu_2O NR sample exhibits a slightly higher efficiency (e.g. at λ = 400 nm, 27% for Cu_2O and 23% for CuO). However, when λ > 400 nm, the IPCE for Cu_2O decreases quickly from 27% to 7% at λ = 500 nm, while for CuO, it decreases very slowly from 23% at λ = 400 nm to 16% at λ = 500 nm. This explains why the J_{ph} of CuO sample is larger than that of Cu_2O samples. By closely examining the IPCE spectra of the three samples, we notice that the IPCE response of Cu_2O/CuO sample almost overlaps with that of the CuO samples when λ > 500 nm while for λ < 400 nm, Cu_2O/CuO and Cu_2O samples have similar spectral shape. In Fig. 8(b) we also plot the sum of the IPCE spectra of single phase CuO and Cu_2O and compare it with that of the mixed phase Cu_2O/CuO. Besides the difference in the magnitude for λ < 550 nm, the spectral shapes are very similar. Clearly the mixed phase Cu_2O/CuO sample greatly enhances the PEC efficiency. Overall, the PEC performance of our Cu_2O/CuO NR (T = 240°C) sample is promising based on the fact that it can be easily fabricated from pure metallic Cu and the composition can be tuned relatively easily. However, the photocurrent density of the best Cu_2O/CuO NR sample is still low when compared to the composite or heterostructured VLAPs reported in the literature, as summarized in Table 3. For more comprehensive details about the single and dual absorber materials including their benchmark values we refer the reader to review papers by Paracchino *et al.*, Moniz *et al.*, and Ager *et al.* [1, 48, 58]

Table 3. Summary of PEC performances for H_2 evolution and/or photocurrrent generation of some of the visible light active photocatalysts.

Photocatalyst	Electrolyte, Potential bias, and Light source	STH% and/or J_{ph} (mA/cm^2)	IPCE value at 400 nm	Ref. Year
Cu_2O/CuO nanorods	0.5M Na_2SO_4, -0.5 V *vs* Ag/AgCl, AM1.5G	0.24 mA/cm^2	44%	Our work
α-Fe_2O_3 nanostructures, with and without (Co-Pi)[a]	Un-buffered NaOH aq. Solution (pH 13.6),1.23 V *vs* RHE, AM1.5G	~ 0.24 mA/cm^2 for α-Fe_2O_3 and 0.435 mA/cm^2 with Co-Pi co-catalyst	--	[59] 2015
CoO nanoparticles	Neutral water, No bias, AM1.5G	~ 5% STH	--	[60] 2014
β-Bi_2O_3 thin film	0.5M Na_2SO_3, AM1.5	0.45 mA/cm^2 at 1.23 V *vs* NHE	43% at 0.197 V *vs* NHE	[61] 2013
$BiVO_4$ (Co-Pi catalyzed)	0.5 M K_2SO_4 (buffered to pH ~ 5.6 with 0.09 M KH_2PO_4/0.01 M K_2HPO_4), 1.23 V *vs* RHE, AM1.5	1.7 mA/cm^2	> 80% between 340 and 420 nm at low light intensities (few μW/cm^2)	[62] 2012
Co-Pi/ $BiVO_4$/WO_3	0.5M Na_2SO_4,1.23 V *vs* RHE, AM1.5	3.2 mA/cm^2	60%	[63] 2014

[a]Co-Pi (Cobalt phosphate)

Conclusions

In summary, we have synthesized the single phase Cu_2O and CuO, and the mixed phase Cu_2O/CuO NR samples with different mass ratios of Cu_2O/CuO by a simple OAD and post-deposition oxidation method. The single phase Cu_2O NRs have both the direct (E_g = 2.54 eV) and indirect (E_g = 2.02 eV) electronic transitions while the single phase CuO samples only exhibit a direct transition (E_g = 2.13 eV). All of the Cu_xO samples are active and efficient in PDD and PEC under the visible light irradiation. A significant enhancement in PDD is observed when aiding the optimal amount of H_2O_2. We have also found that all Cu_xO NR samples are stable in PDD reactions while for PEC performance the single phase CuO NR sample is relatively more stable compared to the both single phase Cu_2O sample and mixed phase Cu_2O/CuO sample. Among the three samples, the mixed phase Cu_2O/CuO sample shows the best PEC performance with photocurrent J_{ph} = -0.24 mA/cm^2 under AM 1.5G, and broad spectra response, with IPCE = 44% at λ = 400 and 10% at λ = 550 nm. Further investigations need to be conducted to reduce or eliminate the degradation effect of the mixed phase Cu_2O/CuO sample in order to achieve a much better performance for photocatalysis and PEC applications.

Experimental Section

Materials

Copper shot (99.9+%) and titanium pellets (99.995 %) were purchased from Alfa Aesar (Ward Hill, MA) and Kurt J. Lesker (Clairton, PA). Cleaned glass microscope slides (Gold Seal ® Catalog No. 3010), indium tin oxide (ITO) coated glass slides (R_s = 8- 12 Ω; Delta Tech. Ltd.) and Si (100) wafers (Montco Silicon Technologies Inc.) were used as substrates for material deposition. High purity methylene blue (MB, $C_{16}H_{18}ClN_3S$; CAS #122965-43-9) and methyl orange (MO, $C_{14}H_{14}N_3NaO_3S$; CAS #547-58-0) were obtained from Alfa-Aesar (Ward Hill, MA). Hydrogen peroxide (H_2O_2, 30% H325-500) solution was purchased from Fisher Scientific (Pittsburgh, PA). Sodium Sulfate, Anhydrous (Na_2SO_4), was purchased from J.T. Baker Chemicals (BAKER ANALYZED, A.C.S. Reagent, 3898-01).

Sample preparation

Both Ti adhesion layer and Cu NR arrays were deposited onto the substrates by a custom designed vacuum deposition system equipped with an electron-beam evaporation source (Torr International, Inc.). The glass, ITO, and Si substrates were cut into the sizes of 9.0 mm × 27.0 mm, 15 mm × 10 mm, and 10.0 mm × 10.0 mm, respectively. Glass substrates were cleaned by a piranha solution using a 4:1 mixture of sulphuric acid (H_2SO_4) and hydrogen peroxide (H_2O_2) solution. Si wafers and ITO substrates were cleaned using a 5:1:1 mixture of deionized (DI) water, H_2O_2, and aqueous ammonia (NH_4OH) solution. Both the glass substrates and the Si wafers were boiled in their respective solutions for 15 minutes before being dried with nitrogen flow. Prior to the deposition, the chamber was evacuated to a base pressure of less than 1×10^{-6} Torr. During the deposition, the pressure was maintained to about ≤ 3×10^{-5} Torr. A 20 nm thick Ti adhesion layer was deposited at the vapour incident angle θ = 0° with respect to

the substrate normal. Then the Cu NRs were deposited at θ = 86°. The deposition rate and thickness were monitored by a quartz crystal microbalance (QCM) positioned directly facing the vapor flux. For both Ti and Cu depositions, the deposition rates were maintained at 0.4 nm/s. For Cu NR arrays, the final QCM thickness reading was 2 μm.

The as-deposited Cu NR samples were then oxidized in a quartz tube furnace (Lindberg/ Blue M Company) at preset temperatures of 150, 190, 210, 240, 290, 340 and 380°C, respectively, in an ambient condition or under oxygen (O_2) flow (20 sccm) to obtain different phases of Cu_xO NRs. During all the treatments, the temperature was ramped at a rate of 5°C/min and the samples were maintained at the final temperature for 3 hours.

Characterization

The morphology and composition of the Cu and Cu_xO NR samples were examined by a field-emission scanning electron microscope (SEM) equipped with an energy dispersive X-ray spectroscopy (FEI Inspect F). The crystal structure of the samples were characterized by a PANalytical X'Pert PRO MRD X-ray diffractometer (XRD) with fixed incidence angle of 0.5°. The XRD patterns were recorded with Cu Kα1 radiation (λ = 1.5405980 Å) in the 2θ range from 20° - 80° at a step size of 0.010°. XRD patterns were used to determine the crystal phase(s), their average crystallite size(s) and the relative wt % of Cu_2O/CuO of the samples oxidized at different temperatures. The optical transmittance of the samples were measured by a double beam UV-visible light (UV-vis) spectrophotometer (JASCO V-570) over a wavelength range from 350 to 850 nm. While the reflectance of the samples were measured at normal incidence using a monochromator and a calibrated beam-splitter (THORLABS Inc. Model: 50/50 BSW26) and baseline correction was done using a silver mirror (THORLABS Inc. Model: PF10-03-P01) using a home built spectrometer system.

Photocatalytic activities of the Cu_xO NR samples were evaluated by the degradation of MB and MO aqueous solutions under visible light irradiation at room temperature (25 ± 2 °C). Note that the detailed photodecay processes of MB and MO are complicated since different reaction products could be produced, leading to conversion of sulfur and nitrogen heteroatoms to sulfate, nitrate, and ammonium ions.[50, 55, 64] A more thorough assessment of the real photocatalytic performance shall require the measurements of the composition of each product as a function of the decay time, and to use the mineralized product of the dye to assess the ultimate photodecay rate.[50, 53] This would be a very tedious process and require advanced instruments. Here we still adapt the general photodecay characterization method that most literature used since the main purpose is to characterize the photodecay performance of materials with similar structure and composition. The starting concentrations of the dyes were chosen to be 31.3 μM for MB and 30.5 μM for MO, and their respective pH values were 6.4 (± 0.2) and 5.7 (± 0.2). The Cu_xO NR samples were placed into a 10 mm × 10 mm × 45 mm clear methacrylate cuvette filled with 3.0 ml of the dye solution. Prior to light irradiation, each sample in the dye solution was remained in dark for 30-60 mins in order for the dye molecules to reach adsorption/desorption equilibrium on NRs. The cuvette was then illuminated by a 250 W quartz halogen lamp (UtiliTech) covering wavelength range from 390 to 850 nm. The illumination area on the samples were fixed as 2.43 cm^2 at a constant light intensity 65 mW/cm^2, as monitored by an optical power meter equipped with a thermal sensor (Thorlabs PM100D/S310C). A water filter was placed in front of the cuvette to absorb the IR light. The photodegradation kinetics of the MB and MO were measured by examining their time dependent characteristic optical absorption peaks, at λ = 664 nm for MB and λ = 465 nm for MO.[4, 33] The time dependent absorption data were fit by a pseudo-first order decay equation, $\alpha(t) = \alpha(0)e^{-\kappa_c t}$, where $\alpha(0)$ is the initial absorbance at time t = 0 min, in order to obtain the decay constant κ_c.

PEC measurements were performed in a home-made single compartment cell with a quartz window (%*T*' >90% in the visible wavelength range) and conventional 3-electrode arrangement using a potentiostat (Pine Instrument AFCBP1 Bipotentiostat). The Cu_xO NR samples deposited on ITO substrates were placed inside the PEC cell, with the deposited NRs facing directly towards illuminating light through the quartz window. The exposure areas were of 1 cm × 1 cm and were used as the working electrodes (WE). An Ag/AgCl electrode (3M KCl) was used as a reference (RE), and a platinum (Pt) coil (diameter ~ 0.5 cm and length ~ 5 cm) was used as a counter electrode (CE). The electrolyte, 0.5 M sodium sulfate (Na_2SO_4) solution, was aerated by N_2 for an hour; the initial pH value of the electrolyte was 6.9 ± 0.2. The CV of the samples were measured in dark at room temperature (25 ± 2 °C), while the photoresponse and IPCE measurements were performed with a solar simulator (AM 1.5G, Oriel instruments, U.S.A., Newport corp. Model# 69911) and a monochromatic light source (APEX, Newport corp. Model: 74100). The illumination area of the monochromator beam, onto the Cu_xO NR samples, was 0.6 cm × 0.4 cm while area of collimated beam from solar simulator was 1 cm × 1 cm. The incident intensity of the solar simulator, at the quartz window of the PEC cell, was adjusted to be 100 mW/cm^2 (1 sun equivalent). And the IPCE measurements were performed from 350 nm to 750 nm at every 10 nm interval. The resolution of the monochromatic source light was adjusted to 2.5 nm. All the PEC measurements were performed under a bias potential of -0.5 V (*vs* Ag/AgCl). Note that the value of bias potentials, *V* (*vs* Ag/AgCl), is not the same as reversible Hydrogen electrode (RHE) or normal Hydrogen electrode (NHE) potentials, but they can be converted according to *V*(RHE or NHE) = *V* + 0.197 V + pH (0.059 V).[27] Therefore, all the potential values listed above are *V* versus Ag/AgCl, unless otherwise stated.

Acknowledgements

Funding for this study was provided by State and Hatch funds allocated to the University of Georgia Agricultural Experiment Station, Griffin Campus and an Agriculture and food Research initiative Grant 2011-68003-30012 from the USDA National Institute of Food and Agriculture, Food Safety: Food Processing Technologies to Destroy Food-borne Pathogens Program-(A4131). The authors would like to thank Dr. G. K. Larsen for proofreading the manuscript.

Notes and references

The authors declare no competing financial interest.

1. A. Paracchino, V. Laporte, K. Sivula, M. Grätzel and E. Thimsen, *Nature Materials*, 2011, **10**, 456-461.
2. A. Kudo and Y. Miseki, *Chemical Society Reviews*, 2009, **38**, 253-278.
3. Z.-G. Zhao and M. Miyauchi, *Angewandte Chemie International Edition*, 2008, **47**, 7051-7055.
4. P. Basnet, G. K. Larsen, R. P. Jadeja, Y.-C. Hung and Y. Zhao, *ACS Appl. Mater. Interfaces*, 2013, **5**, 2085-2095.
5. L. Wang, J. Ge, A. Wang, M. Deng, X. Wang, S. Bai, R. Li, J. Jiang, Q. Zhang, Y. Luo and Y. Xiong, *Angewandte Chemie International Edition*, 2014, **53**, 5107-5111.
6. N. Feng, Q. Wang, A. Zheng, Z. Zhang, J. Fan, S.-B. Liu, J.-P. Amoureux and F. Deng, *Journal of the American Chemical Society*, 2013, **135**, 1607-1616.
7. W. Smith and Y. P. Zhao, *Journal of Physical Chemistry C*, 2008, **112**, 19635-19641.
8. X. Chen, C. Li, M. Grätzel, R. Kostecki and S. S. Mao, *Chemical Society Reviews*, 2012, **41**, 7909-7937.
9. M. Hara, T. Kondo, M. Komoda, S. Ikeda, J. N. Kondo, K. Domen, M. Hara, K. Shinohara and A. Tanaka, *Chemical Communications*, 1998, 357-358.
10. G. Ren, D. Hu, E. W. C. Cheng, M. A. Vargas-Reus, P. Reip and R. P. Allaker, *International Journal of Antimicrobial Agents*, 2009, **33**, 587-590.
11. J. C. Park, J. Kim, H. Kwon and H. Song, *Advanced Materials*, 2009, **21**, 803-807.
12. B. K. Meyer, A. Polity, D. Reppin, M. Becker, P. Hering, P. J. Klar, T. Sander, C. Reindl, J. Benz, M. Eickhoff, C. Heiliger, M. Heinemann, J. Bläsing, A. Krost, S. Shokovets, C. Müller and C. Ronning, *physica status solidi (b)*, 2012, **249**, 1487-1509.
13. M. Yin, C.-K. Wu, Y. Lou, C. Burda, J. T. Koberstein, Y. Zhu and S. O'Brien, *Journal of the American Chemical Society*, 2005, **127**, 9506-9511.
14. A. S. Zoolfakar, R. A. Rani, A. J. Morfa, A. P. O'Mullane and K. Kalantar-zadeh, *Journal of Materials Chemistry C*, 2014, **2**, 5247-5270.
15. M. Heinemann, B. Eifert and C. Heiliger, *Phys Rev B*, 2013, **87**, 115111.
16. H. Yu, J. Yu, S. Liu and S. Mann, *Chem Mater*, 2007, **19**, 4327-4334.
17. J. Zhang, J. Liu, Q. Peng, X. Wang and Y. Li, *Chem Mater*, 2006, **18**, 867-871.
18. W. Chen, Z. Fan and Z. Lai, *Journal of Materials Chemistry A*, 2013, **1**, 13862-13868.
19. P. E. de Jongh, D. Vanmaekelbergh and J. J. Kelly, *J Electrochem Soc*, 2000, **147**, 486-489.
20. B. Zhou, Z. Liu, H. Wang, Y. Yang and W. Su, *Catal Lett*, 2009, **132**, 75-80.
21. P. E. de Jongh, D. Vanmaekelbergh and J. J. Kelly, *Chemical Communications*, 1999, 1069-1070.
22. L. Wu, L.-k. Tsui, N. Swami and G. Zangari, *Journal of Physical Chemistry C*, 2010, **114**, 11551-11556.
23. S. Emin, F. F. Abdi, M. Fanetti, W. Peng, W. Smith, K. Sivula, B. Dam and M. Valant, *Journal of Electroanalytical Chemistry*, 2014, **717–718**, 243-249.
24. Z. Zhang and P. Wang, *J Mater Chem*, 2012, **22**, 2456-2464.
25. L. I. Bendavid and E. A. Carter, *Journal of Physical Chemistry B*, 2013, **117**, 15750-15760.
26. X. P. Gao, J. L. Bao, G. L. Pan, H. Y. Zhu, P. X. Huang, F. Wu and D. Y. Song, *Journal of Physical Chemistry B*, 2004, **108**, 5547-5551.
27. Y.-F. Lim, C. S. Chua, C. J. J. Lee and D. Chi, *Physical chemistry chemical physics : PCCP*, 2014, **16**, 25928-25934.
28. H. F. Li, A. K. Kar, T. Parker, G. C. Wang and T. M. Lu, *Nanotechnology*, 2008, **19**, 335708.
29. V. Figueiredo, E. Elangovan, G. Goncalves, P. Barquinha, L. Pereira, N. Franco, E. Alves, R. Martins and E. Fortunato, *Appl Surf Sci*, 2008, **254**, 3949-3954.
30. J. Deuermeier, J. Gassmann, J. Brötz and A. Klein, *Journal of Applied Physics*, 2011, **109**, 113704.
31. D. Nunes, A. Pimentel, P. Barquinha, P. A. Carvalho, E. Fortunato and R. Martins, *Journal of Materials Chemistry C*, 2014, **2**, 6097-6103.
32. X. C. Jiang, T. Herricks and Y. N. Xia, *Nano Letters*, 2002, **2**, 1333-1338.
33. P. Basnet and Y. Zhao, *Journal of Materials Chemistry A*, 2014, **2**, 911-914.
34. A. Wolcott, W. A. Smith, T. R. Kuykendall, Y. P. Zhao and J. Z. Zhang, *Small*, 2009, **5**, 104-111.
35. J. Steele and M. Brett, *Journal of Materials Science: Materials in Electronics*, 2007, **18**, 367-379.
36. Y. He, P. Basnet, S. E. H. Murph and Y. Zhao, *ACS Appl. Mater. Interfaces*, 2013, **5**, 11818-11827.
37. W. Smith, A. Wolcott, R. C. Fitzmorris, J. Z. Zhang and Y. Zhao, *J Mater Chem*, 2011, **21**, 10792-10800.
38. I. Hodgkinson, Q. H. Wu and J. Hazel, *Applied Optics*, 1998, **37**, 2653-2659.
39. R. N. Tait, T. Smy and M. J. Brett, *Thin Solid Films*, 1993, **226**, 196-201.
40. H. Zhu, W. Cao, G. K. Larsen, R. Toole and Y. Zhao, *J Vac Sci Technol B*, 2012, **30**, 030606.
41. C. Suryanarayana, *Progress in Materials Science*, 2001, **46**, 1-184.
42. R. Köferstein, *J Alloy Compd*, 2014, **590**, 324-330.
43. J. Rodríguez-Carvajal, *Physica B: Condensed Matter*, 1993, **192**, 55-69.
44. D. Channei, B. Inceesungvorn, N. Wetchakun, S. Ukritnukun, A. Nattestad, J. Chen and S. Phanichphant, *Sci. Rep.*, 2014, **4**.
45. N. Wetchakun, S. Chaiwichain, B. Inceesungvorn, K. Pingmuang, S. Phanichphant, A. I. Minett and J. Chen, *ACS Appl. Mater. Interfaces*, 2012, **4**, 3718-3723.
46. R. Asahi, T. Morikawa, T. Ohwaki, K. Aoki and Y. Taga, *Science*, 2001, **293**, 269-271.
47. G. Ghadimkhani, N. R. de Tacconi, W. Chanmanee, C. Janaky and K. Rajeshwar, *Chemical Communications*, 2013, **49**, 1297-1299.
48. S. J. A. Moniz, S. A. Shevlin, D. J. Martin, Z.-X. Guo and J. Tang, *Energy & Environmental Science*, 2015, **8**, 731-759.
49. T. Hisatomi, J. Kubota and K. Domen, *Chemical Society Reviews*, 2014, **43**, 7520-7535.
50. A. Houas, H. Lachheb, M. Ksibi, E. Elaloui, C. Guillard and J. M. Herrmann, *Applied Catalysis B-Environmental*, 2001, **31**, 145-157.
51. J. Jiang, K. Zhao, X. Xiao and L. Zhang, *Journal of the American Chemical Society*, 2012, **134**, 4473-4476.
52. I. K. Konstantinou and T. A. Albanis, *Applied Catalysis B-Environmental*, 2004, **49**, 1-14.
53. M. Neamtu, H. Siminiceanu, A. Yediler and A. Kettrup, *Dyes and Pigments*, 2002, **53**, 93-99.
54. A. Mills and J. S. Wang, *Journal of Photochemistry and Photobiology a-Chemistry*, 1999, **127**, 123-134.
55. M. Aslam, I. M. I. Ismail, S. Chandrasekaran, H. A. Qari and A. Hameed, *Water Air and Soil Pollution*, 2015, **226**.

56. S. Chen and L.-W. Wang, *Chem Mater*, 2012, **24**, 3659-3666.
57. L. Chen, S. Shet, H. Tang, H. Wang, T. Deutsch, Y. Yan, J. Turner and M. Al-Jassim, *J Mater Chem*, 2010, **20**, 6962-6967.
58. J. W. Ager iii, M. Shaner, K. Walczak, I. D. Sharp and S. Ardo, *Energy & Environmental Science*, 2015.
59. M. E. A. Warwick, K. Kaunisto, D. Barreca, G. Carraro, A. Gasparotto, C. Maccato, E. Bontempi, C. Sada, T.-P. Ruoko, S. Turner and G. Van Tendeloo, *ACS Appl. Mater. Interfaces*, 2015, **7**, 8667-8676.
60. L. Liao, Q. Zhang, Z. Su, Z. Zhao, Y. Wang, Y. Li, X. Lu, D. Wei, G. Feng, Q. Yu, X. Cai, J. Zhao, Z. Ren, H. Fang, F. Robles-Hernandez, S. Baldelli and J. Bao, *Nature Nanotechnology*, 2014, **9**, 69-73.
61. X. Yang, X. Lian, S. Liu, G. Wang, C. Jiang, J. Tian, J. Chen and R. Wang, *Journal of Physics D-Applied Physics*, 2013, **46**.
62. F. F. Abdi and R. van de Krol, *Journal of Physical Chemistry C*, 2012, **116**, 9398-9404.
63. Y. Pihosh, I. Turkevych, K. Mawatari, T. Asai, T. Hisatomi, J. Uemura, M. Tosa, K. Shimamura, J. Kubota, K. Domen and T. Kitamori, *Small*, 2014, **10**, 3692-3699.
64. H. Lachheb, E. Puzenat, A. Houas, M. Ksibi, E. Elaloui, C. Guillard and J. M. Herrmann, *Applied Catalysis B-Environmental*, 2002, **39**, 75-90.